IEEE Access
Multidisciplinary ⋮ Rapid Review ⋮ Open Access Journal

Received March 10, 2022, accepted March 26, 2022, date of publication April 5, 2022, date of current version April 12, 2022.

Digital Object Identifier 10.1109/ACCESS.2022.3165054

Electric Vehicle State Parameter Estimation Based on DICI-GFCKF

ZHANG RONGYUN[1], LIU YAMING[1], SHI PEICHENG[2], ZHAO LINFENG[3], DU YUFENG[1], AND FENG YONGLE[1]

[1]School of Mechanical Engineering, Anhui Polytechnic University, Wuhu 241000, China
[2]Automotive New Technology Anhui Engineering and Technology Research Center, Anhui Polytechnic University, Wuhu 241000, China
[3]School of Automotive and Transportation Engineering, Hefei University of Technology, Hefei 230009, China

Corresponding author: Zhang Rongyun (hanfengzhiwei@163.com)

This work was supported in part by the National Natural Science Foundation of China under Grant 51605003 and Grant 51575001, in part by the Natural Science Foundation of the Anhui Higher Education Institutions of China under Grant KJ2020A0358, and in part by the Young and Middle-Aged Top Talents Training Program of Anhui Polytechnic University.

ABSTRACT To improve the estimation accuracy of the state parameters of distributed electric vehicles, a double inverse covariance intersection generalized fifth-order cubature Kalman filter (DICI-GFCKF) estimation algorithm is proposed. Based on the fifth-order cubature Kalman filter algorithm, the generalized cubature rule is used to directly obtain the weight and cubature point of the algorithm. Then, the inverse covariance intersection (ICI) data fusion algorithm is introduced and combined with the generalized fifth-order CKF, and the double inverse covariance intersection-generalized fifth-order cubature Kalman filter is derived. The algorithm is applied to estimate the state parameters of distributed electric vehicles. Finally, the simulation and the vehicle experiment show that the algorithm not only improves the estimation accuracy and stability but also reduces the influence of the system model nonlinearity on the algorithm, and has good effectiveness and robustness.

INDEX TERMS Electric vehicles, state parameter estimation, generalized cubature rule, ICI data fusion, fifth-order CKF.

I. INTRODUCTION

The electric vehicle sector has developed exponentially in China in the last few years as one of the most essential strategies for achieving energy transition. As a very important part of electrical vehicles, the driving force and braking force of the motor are independently governable, with a high control accuracy and a quick response speed [1]–[3]. The main development trend in intelligent vehicle power transmission is the distributed electric drive. Additionally, precisely gaining vehicle driving state parameters is the foundation for smart vehicles to make accurate control and decisions. Because of the cost and the technological constraints, a reliable and stable algorithm for estimating a vehicle's sideslip angle, yaw rate, and other difficult-to-gain state characteristics is needed.

Accurate estimates of vehicle driving state parameters have always been a common issue for researchers. The unscented Kalman filter (UKF) [4]–[7] and the extended Kalman filter (EKF) [8]–[10] are now the most popular algorithms for estimating vehicle state parameters, while some researchers also employ the cubature Kalman filter (CKF) [11], [12] and the particle filter (PF) [13], [14]. H. Heidfeld *et al.*, considering the uncertainty of the tire model, used the unscented Kalman filter to estimate the sideslip angle and the tire parameters [15]. J. Xianjian *et al.* observed the vehicle speed, the sideslip angle, and the vehicle inertia coefficient through the unscented Kalman filter [16]. T. Kim *et al.* proposed a method combining LIDAR and the extended Kalman filter, which improved the accuracy of the distance measurement, and reduced the error of the algorithm [17]. W. Shaoyuan *et al.* used singular value decomposition to improve the cubature Kalman filter and estimated the lateral velocity, the longitudinal velocity, and the sideslip angle [18]. Katriniok *et al.* used the extended Kalman filter to dynamically observe vehicle longitudinal and lateral velocities, as well as the yaw rate, and proved that the filter had such good estimation accuracy through real vehicle experiments [19]. S. Strano *et al.* proposed a constrained untraced Kalman filter (CUKF) to estimate the sideslip angle by considering the state constraints of the unscented Kalman filter in the estimation process [20].

The associate editor coordinating the review of this manuscript and approving it for publication was Halil Ersin Soken.

The UKF has strong estimating capabilities for nonlinear systems, but it is prone to losing accuracy and collapsing the algorithm when dealing with high-dimensional matrices.

The EKF is a reliable way to estimate a vehicle's sideslip angles. To linearize the system, the method must execute the Jacobian matrix derivation of the state equation. As a result, the extent of the computation is vast for nonlinear systems, and the error is larger. A genetic algorithm improves the PF, and the particle shortage problem is overcome. The calculated value outperforms the UKF and the UPF-derived values in an experimental comparison. This approach generates a large number of particles, consumes computer memory, slows down computation, and results in poor real-time performance. Arasaratnm and Haykin proposed a cubature Kalman filter (CKF) algorithm based on the cubature rule [21]. Compared with UKF and EKF, the CKF obtains higher accuracy by integrating the spherical and radial surfaces, respectively, by using the spherical-radial cubature rule. However, the third-order CKF is not sufficiently accurate in many filtering problems. To obtain the state parameters of the vehicle more accurately, a higher-order CKF is needed to improve its performance. However, the complex structure of the spherical-radial integral used in the third-order CKF makes it difficult to derive a higher-order CKF. Therefore, this paper proposes a high-order CKF algorithm that uses the properties of a fully symmetric numerical integral equation to solve the weight and cubature points of the cubature equation, and then constructs the CKF algorithm of different orders.

In summary, the above problem of the lack of accuracy in estimating the driving state parameters of distributed electric vehicles is addressed. In this paper, a nonlinear vehicle dynamics model is established, and a discrete mathematical model for the estimation algorithm is obtained. Using the generalized cubature rule and the ICI data fusion algorithm, a generalized fifth-order CKF algorithm with double ICI fusion is proposed to estimate the state parameters of the distributed drive electric vehicles. To prove the effectiveness of the proposed algorithm, joint simulation and actual vehicle experiments are carried out in the MATLAB/Simulink and Carsim software. The results show that the estimation algorithm proposed in this paper has high accuracy.

This paper is organized as follows: Section 2 presents the system model, which includes the 3-degree-of-freedom vehicle dynamics model and the lateral force estimation model. The local fusion algorithm and the DICI-GFCKF algorithm are described in Section 3 and Section 4. Section 5 presents the simulation analysis, and the real vehicle experiment is presented in Section 6. The concluding remarks are presented in Section 7.

II. NONLINEAR VEHICLE DYNAMICS MODEL

A. THREE-DEGREES OF FREEDOM VEHICLE DYNAMICS MODEL

A nonlinear 3-DOF vehicle model is built to make it easier to predict the vehicle state, as shown in Figure 1 [22], [23].

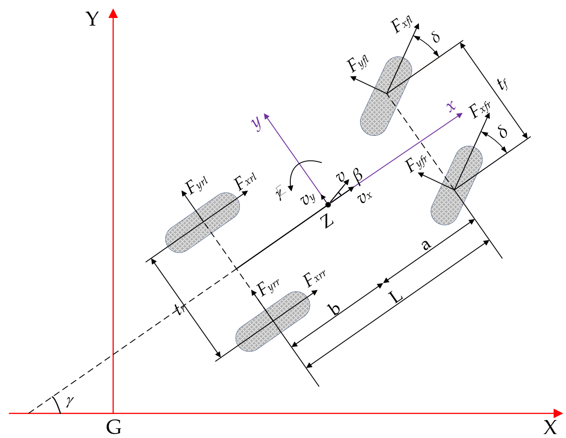

FIGURE 1. Vehicle dynamics model.

The equilibrium equation of vehicle dynamics is as follows:

$$\begin{aligned} a_x &= \frac{1}{m}[(F_{xfl}+F_{xfr})\cos\delta-(F_{yfl}+F_{yfr})\sin\delta \\ &\quad +F_{xrl}+F_{xrr}] \end{aligned} \tag{1}$$

$$\begin{aligned} a_y &= \frac{1}{m}[(F_{xfl}+F_{xfr})\sin\delta+(F_{yfl}+F_{yfr})\cos\delta \\ &\quad +F_{yrl}+F_{yrr}] \end{aligned} \tag{2}$$

$$\begin{aligned} I_z\dot{\gamma} &= [(F_{xfr}-F_{xfl})\cos\delta+(F_{yfl}-F_{yfr})\sin\delta]\frac{t_f}{2} \\ &\quad +[(F_{xfl}+F_{xfr})\sin\delta \\ &\quad +(F_{yfr}+F_{yfl})\cos\delta]a+(F_{xrr} \\ &\quad -F_{xrl})\frac{t_f}{2}-(F_{yrr}+F_{yrl})b \end{aligned} \tag{3}$$

where γ is the yaw rate, β is the sideslip angle, δ is the front wheel angle, m is the mass of the vehicle, I_z is the moment of inertia about the z-axis, the tires' longitudinal and lateral forces are F_{xij} and F_{yij}, the front and rear wheel treads are t_f and t_r, and the distances between the center of the centroid position and the front and rear axles are a and b.

B. LATERAL FORCE ESTIMATION MODEL

The distributed drive electric vehicle is the subject of this study. The four-wheel longitudinal force may be calculated directly using the driving torque and the motor speed as follows [24]–[26]:

$$\hat{F}_{xij} = (T_{ij}-J\omega_{ij})/R \tag{4}$$

where J denotes the four-wheel moment of inertia, T_{ij} denotes the four-wheel driving torque, ω_{ij} denotes the four-wheel wheel speed, and R denotes the wheel radius.

Using the magic tire model to calculate the lateral force, the formula is as follows:

$$\begin{aligned} \hat{F}_{yij} &= D\sin[C\arctan\{BX-E(BX-\arctan(BX))\}] \\ X &= x+S_h \end{aligned} \tag{5}$$

This equation is very adaptable to a static vehicle system. However when the vehicle speed or tires' sideslip angle varies due to the changing road conditions, the lateral force computed by the magic formula is too inaccurate. As a result, the relaxation model is used in this article to estimate the wheel lateral force, which is indicated in the equation as follows [27]:

$$\dot{F}_{yij} = \frac{\sqrt{v_x^2 + (v_x\beta)^2}}{\sigma_{ij}}(F_{yij} - \hat{F}_{yij}) \tag{6}$$

where σ_{ij} is the relaxation factor, S_h is the horizontal displacement, B is the rigidity factor, C is the shape factor, D is the peak factor, and E is the curvature factor.

The vertical load of the wheels is related to each element in the equation above. The change in the tire force is caused by a change in the vertical load of the wheel and the sideslip angle of the tire. Therefore, the normal forces and the sideslip angle of the tire must be calculated as follows:

$$\begin{aligned} F_{zfl,r} &= m(g\frac{b}{2(a+b)} - a_x\frac{h_g}{2(a+b)} \mp a_y\frac{h_g b}{t_f(a+b)}) \\ F_{zrl,r} &= m(g\frac{a}{2(a+b)} + a_x\frac{h_g}{2(a+b)} \mp a_y\frac{h_g a}{t_r(a+b)}) \end{aligned} \tag{7}$$

$$\begin{aligned} \alpha_{fl,r} &= \delta - \arctan(\frac{v_y + a\gamma}{v_x \mp \frac{t_f}{2}\gamma}) \\ \alpha_{rl,r} &= -\arctan(\frac{v_y - b\gamma}{v_x \mp \frac{t_r}{2}\gamma}) \end{aligned} \tag{8}$$

where γ is the yaw rate, F_{zij} is the tire's normal force, h_g is the center of the mass height, and α_{ij} is the sideslip angle of the tire.

C. STATE SPACE REPRESENTATION

To calculate the yaw rate, the sideslip angle, and the longitudinal speed, according to (1-3), the state equation and the measurement equation are established as follows:

$$\begin{cases} \dot{\boldsymbol{x}}_a(t) = f_a(\boldsymbol{x}_a(t), \boldsymbol{u}_a(t)) + \boldsymbol{w}_a(t) \\ z_a(t) = h_a(\boldsymbol{x}_a(t), \boldsymbol{u}_a(t)) + \boldsymbol{v}_a(t) \end{cases} \tag{9}$$

where the state variable $\boldsymbol{x}_a(t) = (\gamma, \beta, v_x)^T = (x_{a1}, x_{a2}, x_{a3})^T$; the measured variable $\boldsymbol{z}_a(t) = (a_y) = (z_{a1})$; and the input variable $\boldsymbol{u}_a(t) = (\delta, a_x)^T = (u_{a1}, u_{a2})^T$. The function f_a can be expressed as follows:

$$f_a = \begin{bmatrix} \frac{k_1a^2 + k_2b^2}{I_z x_{a3}}x_{a1} + \frac{k_1a - k_2b}{I_z}x_{a2} - \frac{k_1a}{I_z}u_{a1} \\ \frac{k_1a - k_2b - mx_{a3}^2}{mx_{a3}^2}x_{a1} + \frac{k_1 + k_2}{mv_x}x_{a2} - \frac{k_1}{mv_x}u_{a1} \\ x_{a1}x_{a2}x_{a3} + u_{a2} \end{bmatrix} \tag{10}$$

The function h_a can be expressed as follows:

$$h_a = \frac{ak_1 - bk_2}{mx_{a3}}x_{a1} + \frac{k_1 + k_2}{m}x_{a2} - \frac{k_1}{m}u_{a1} \tag{11}$$

The state equation and the measurement equation of the wheel lateral force can be established according to (4-8) as follows:

$$\begin{cases} \dot{\boldsymbol{x}}_b(t) = f_b(\boldsymbol{x}_b(t), \boldsymbol{u}_b(t)) + \boldsymbol{w}_b(t) \\ z_b(t) = h_b(\boldsymbol{x}_b(t), \boldsymbol{u}_b(t)) + \boldsymbol{v}_b(t) \end{cases} \tag{12}$$

where the state variable $\boldsymbol{x}_b(t) = (F_{yfl}, F_{yfr}, F_{yrl}, F_{yrr})^T = (x_{b1}, x_{b2}, x_{b3}, x_{b4})^T$; the measured variable $\boldsymbol{z}_b(t) = (a_x, a_y)^T = (z_{b1}, z_{b2})^T$; and the input variable $\boldsymbol{u}_b(t) = (\delta, v_x, \beta, F_{xfl}, F_{xfr}, F_{xrl}, F_{xrr})^T = (u_{b1}, u_{b2}, u_{b3}, u_{b4}, u_{b5}, u_{b6}, u_{b7})^T$. The function f_b can be expressed as follows:

$$f_b = \begin{bmatrix} \frac{u_{b2}\sqrt{1+u_{b3}^2}}{\sigma_{ij}}(x_{b1} - \hat{F}_{yfl}) \\ \frac{u_{b2}\sqrt{1+u_{b3}^2}}{\sigma_{ij}}(x_{b2} - \hat{F}_{yfr}) \\ \frac{u_{b2}\sqrt{1+u_{b3}^2}}{\sigma_{ij}}(x_{b3} - \hat{F}_{yrl}) \\ \frac{u_{b2}\sqrt{1+u_{b3}^2}}{\sigma_{ij}}(x_{b4} - \hat{F}_{yrr}) \end{bmatrix} \tag{13}$$

The function h_b can be expressed as follows: (14), as shown at the bottom of the next page.

III. LOCAL FUSION ALGORITHM

For the local fusion problem of a vehicle's multisensor system, its cross-covariance matrix is often difficult to obtain, but the CI algorithm provides a good solution to data fusion in the case of unknown cross-covariance.

The CI fusion algorithm is as follows:

For j = 1, … n vehicle-mounted multisensor systems, the local estimate $\hat{\boldsymbol{x}}_j$ and the corresponding error covariance matrix $\boldsymbol{P}_j$ are known. The CI fusion algorithm is as follows:

$$\begin{aligned} \hat{\boldsymbol{x}}_{CI} &= \boldsymbol{P}_{CI}\sum_{j=1}^{n}\omega_j\boldsymbol{P}_j^{-1}\hat{\boldsymbol{x}}_j \\ \boldsymbol{P}_{CI}^{-1} &= \sum_{j=1}^{n}\omega_j\boldsymbol{P}_j^{-1} \\ &\sum_{j=1}^{n}\omega_j = 1 \end{aligned} \tag{15}$$

The minimization parameter ω_j is determined by the equation as follows:

$$\min\ tr\boldsymbol{P}_{CI} = \min_{\omega\in[0,1]} tr\left\{[\sum_{j=1}^{n}\omega_j\boldsymbol{P}_j^{-1}]^{-1}\right\} \tag{16}$$

However, the CI fusion algorithm has strong limitations, and the fusion results obtained by this algorithm are conservative. Reference [28] proposed the inverse covariance intersection (ICI) fusion algorithm, which not only inherits the advantages of the CI fusion algorithm but also greatly reduces its conservatism and improves the fusion accuracy, which is an improvement of the CI fusion algorithm.

The ICI fusion algorithm is written as follows:

$$\hat{\boldsymbol{x}}_{ICI} = \sum_{j=1}^{n} L_j \hat{\boldsymbol{x}}_j \tag{17}$$

where the gains $L_1 \ldots L_n$ are as follows:

$$L_j = \boldsymbol{P}_{ICI}(\boldsymbol{P}_j^{-1} - \omega_j(\sum_{j=1}^{n} \omega_j \boldsymbol{P}_j)^{-1}) \quad j = 1, \cdots, n \tag{18}$$

The ICI fusion error variance matrix is as follows:

$$\boldsymbol{P}_{ICI} = (\sum_{j=1}^{n} \boldsymbol{P}_j^{-1} - (\sum_{j=1}^{n} \omega_j \boldsymbol{P}_j)^{-1})^{-1} \tag{19}$$

The minimization parameter ω_j is determined by the equation as follows:

$$\min tr\boldsymbol{P}_{ICI} = \min_{\omega \in [0,1]} tr \left\{ [\sum_{j=1}^{n} \boldsymbol{P}_j^{-1} - (\sum_{j=1}^{n} \omega_j \boldsymbol{P}_j)^{-1}]^{-1} \right\}$$

$$\sum_{j=1}^{n} \omega_j = 1 \tag{20}$$

This paper combines the ICI fusion algorithm with the Kalman filter algorithm to obtain the double inverse covariance intersection-generalized fifth-order cubature Kalman filter. This algorithm avoids the estimation error caused by the unknown mutual covariance matrix between the sensors. The traditional error covariance matrix ($\boldsymbol{P}_k$) is updated by the ICI fused error covariance matrix ($\boldsymbol{P}_{ICI}$). Errors in the update process of the Kalman filter algorithm are reduced, and the accuracy and the robustness of the filter are improved.

IV. THE DICI-GFCKF ALGORITHM

The state equation and the observation equation of the vehicle filter are established as follows:

$$\begin{cases} \boldsymbol{x}(k+1) = f(\boldsymbol{x}(k), \boldsymbol{u}(k)) + \boldsymbol{w}(k) \\ z(k+1) = h(\boldsymbol{x}(k+1), \boldsymbol{u}(k+1)) + \boldsymbol{v}(k+1) \end{cases} \tag{21}$$

where $\boldsymbol{x}(k) \in \boldsymbol{R}^n$ is the system state, $\boldsymbol{u}(k) \in \boldsymbol{R}^m$ and $\boldsymbol{z}(k+1) \in \boldsymbol{R}^p$ represent the control input and the measurement vector at discrete time $k+1$. $f(.)$ represents the system function and h denotes the measurement function. $\boldsymbol{w}(k)$ and $\boldsymbol{v}(k+1)$ denote the process and the measurement noise with a known covariance, $\boldsymbol{w}(k) \sim N(0, \boldsymbol{Q})$ and $\boldsymbol{v}(k+1) \sim N(0, \boldsymbol{R})$.

A. GENERALIZED CUBATURE RULE

The fifth-order CKF is first processed using the generalized cubature rule, and then the ICI algorithm is merged into it to increase the accuracy of the vehicle state estimate. Finally, the DICI-GFCKF (double inverse covariance intersection generalized fifth-order cubature Kalman filter) is constructed.

The equation for the generalized cubature rule is as follows [29]–[31]:

$$\begin{aligned} I(f) &= \int_{R^n} f(x) N(x; \hat{x}, P) \\ &= \tilde{W}_0 f[0] + \tilde{W}_1 \sum_{i=1}^{2n} f[\tau] + \tilde{W}_{1,1} \sum_{i=1}^{2n(n-1)} f[\tau, \tau], n > 1 \end{aligned} \tag{22}$$

where $\tilde{W}_0$, $\tilde{W}_1$, $\tilde{W}_{1,1}$ are the weights of $f[0]$, $f[\tau]$, and $f[\tau, \tau]$, which satisfy the following equation as follows:

$$\begin{bmatrix} I_0 \\ I_2 \\ I_4 \\ I_{2,2} \end{bmatrix} = \begin{bmatrix} \tilde{W}_0 + 2n\tilde{W}_1 + 2n(n-1)\tilde{W}_{1,1} \\ 2\upsilon^2 \tilde{W}_1 + 4(n-1)\upsilon^2 \tilde{W}_{1,1} \\ 2\upsilon^4 \tilde{W}_1 + 4(n-1)\upsilon^4 \tilde{W}_{1,1} \\ 4\upsilon^4 \tilde{W}_{1,1} \end{bmatrix} \tag{23}$$

The solution to (23) is as follows:

$$\begin{cases} I_0 = \int_{R^n} \exp(-x^T x) dx = \sqrt{\pi^n} \\ I_2 = \int_{R^n} \exp(-x^T x) dx = \sqrt{\pi^n}/2 \\ I_4 = \int_{R^n} x_1^4 \exp(-x^T x) dx = 3\sqrt{\pi^n}/4 \\ I_{2,2} = \int_{R^n} x_1^2 x_2^2 \exp(-x^T x) dx = \sqrt{\pi^n}/4 \end{cases} \tag{24}$$

The unique solution to (24) is as follows:

$$\begin{aligned} \tau &= \sqrt{\frac{3}{2}} \\ \tilde{W}_0 &= [1 - (7-n)n/18]/\sqrt{\pi^n} \\ \tilde{W}_1 &= (4-n)\sqrt{\pi^n}/18, \quad \tilde{W}_2 = \sqrt{\pi^n}/36 \end{aligned} \tag{25}$$

Substituting the solution into (22) is as follows:

$$\begin{aligned} I(f) &= \int_{R^n} f(x) N(x; \hat{x}, P) \\ &= (1 - \frac{(7-n)n}{18}) f([0]) + \frac{4-n}{18} \sum_{i=1}^{2n} f([\sqrt{3}]_i) \\ &\quad + \frac{1}{36} \sum_{i=1}^{2n(n-1)} f([\sqrt{3}, \sqrt{3}]_i) \end{aligned} \tag{26}$$

The cubature points and the weights of the GFCKF algorithm can be obtained by (26) as follows:

$$\begin{aligned} \xi_i &= \begin{cases} [0]_i i = 1 \\ [\sqrt{3}]_i i = 2, \cdots, 2n+1 \\ [\sqrt{3}, \sqrt{3}]_i i = 2(n+2), \cdots, 2n^2+1 \end{cases} \\ W_i &= \begin{cases} 1 - (7-n)n/18, \; i = 1 \\ (4-n)/18, \quad i = 2, \cdots, 2n+1 \\ 1/36, \quad i = 2(n+2), \cdots, 2n^2+1 \end{cases} \end{aligned} \tag{27}$$

$$h_b = \begin{bmatrix} [(u_{b4} + u_{b5}) \cos u_{b1} - (x_{b1} + x_{b2}) \sin u_{b1} + u_{b6} + u_{b7}]/m \\ [(u_{b4} + u_{b5}) \sin u_{b1} + (x_{b1} + x_{b2}) \cos u_{b1} + x_{b3} + x_{b4}]/m \end{bmatrix} \tag{14}$$

B. DICI-GFCKF

The weights and the cubature points of the DICI-GFCKF algorithm are calculated according to the generalized cubature rule, and the algorithm steps are as follows [32], [33]:

1) TIME UPDATE CALCULATION

① Set initial values ($\boldsymbol{P}_{j\,k}$, $\boldsymbol{S}_{j\,k}$ and W_i) and calculate the cubature points as follows:

$$\boldsymbol{x}_{jk,i} = \hat{\boldsymbol{x}}_{jk} + \boldsymbol{S}_{jk}\boldsymbol{\xi}_i \quad i = 1, \cdots, 2n^2+1 \tag{28}$$

where $\boldsymbol{S}_{jk}$ is the matrix obtained from the Cholesky decomposition of $\boldsymbol{P}_{j\,k}$, as follows:

$$\boldsymbol{P}_{jk} = \boldsymbol{S}_{jk}\boldsymbol{S}_{jk}^T \quad j = 1, 2, \cdots, n$$

② Obtain propagated cubature points as follows:

$$\boldsymbol{x}_{jk+1/k,i} = f(\boldsymbol{x}_{jk,i}, \boldsymbol{u}_{jk}) \tag{29}$$

③ Calculate the value of the state prediction as follows:

$$\hat{\boldsymbol{x}}_{jk+1/k} = \sum_{i=1}^{2n^2+1} W_i \boldsymbol{x}_{jk+1/k,i} \tag{30}$$

④ Update the covariance matrix as follows:

$$\boldsymbol{P}_{jk+1/k} = \sum_{i=1}^{2n^2+1} W_i(\boldsymbol{x}_{jk+1/k,i} - \hat{\boldsymbol{x}}_{jk+1/k})(\boldsymbol{x}_{jk+1/k,i} - \hat{\boldsymbol{x}}_{j\,k+1/k})^T + \boldsymbol{Q}_{jk} \tag{31}$$

2) ICI PRIMARY FUSION

① Calculate the prior covariance square root of the system as follows:

$$\boldsymbol{P}_{k+1/k}^{ICI} = (\sum_{j=1}^{n} \boldsymbol{P}_{j\,k+1/k}^{-1} - (\sum_{j=1}^{n} \omega_j \boldsymbol{P}_{j\,k+1/k})^{-1})^{-1} \tag{32}$$

② Calculate gains $L_1 \ldots L_n$ as follows:

$$L_j = \boldsymbol{P}_{k+1/k}^{ICI}(\boldsymbol{P}_{jk+1/k}^{-1} - \omega_j(\sum_{j=1}^{n} \omega_j \boldsymbol{P}_{j\,k+1/k})^{-1}) \tag{33}$$

③ Calculate the state prediction value of the system as follows:

$$\hat{\boldsymbol{x}}_{k+1/k}^{ICI} = \sum_{j=1}^{n} L_j \hat{\boldsymbol{x}}_{jk+1/k} \tag{34}$$

3) MEASURING UPDATE

① Calculate the new cubature points as follows:

$$\boldsymbol{x}_{jk+1/k,i} = \boldsymbol{P}_{k+1/k}^{ICI}\boldsymbol{\xi}_i + \hat{\boldsymbol{x}}_{k+1/k}^{ICI} \quad i = 1, \cdots, 2n^2+1 \tag{35}$$

② Based on the measured factors, create new cubature points as follows:

$$\boldsymbol{y}_{jk+1,i} = h(\boldsymbol{x}_{jk+1/k,i}, \boldsymbol{u}_{jk}) \tag{36}$$

③ The measurement's predicted value is as follows:

$$\hat{z}_{jk+1} = \sum_{i=1}^{2n^2+1} W_i \boldsymbol{y}_{jk+1,i} \tag{37}$$

④ Apply the cross-covariance and innovation covariance as follows:

$$\begin{aligned}\boldsymbol{P}_{jk+1/k}^{xz} &= \sum_{i=1}^{2n^2+1} W_i(\boldsymbol{x}_{jk+1/k,i} - \hat{\boldsymbol{x}}_{j\,k+1/k})(\boldsymbol{y}_{jk+1,i} - \hat{z}_{jk+1})^T \\ \boldsymbol{P}_{jk+1}^{zz} &= \sum_{i=1}^{2n^2+1} W_i(\boldsymbol{y}_{jk+1,i} - \hat{z}_{jk+1})(\boldsymbol{y}_{jk+1,i} - \hat{z}_{jk+1})^T + \boldsymbol{R}_{jk}\end{aligned} \tag{38}$$

⑤ Obtain the filter gain matrix as follows:

$$\boldsymbol{K}_{jk+1} = \boldsymbol{P}_{jk+1/k}^{xz}(\boldsymbol{P}_{jk+1}^{zz})^{-1} \tag{39}$$

⑥ Perform the state estimate as follows:

$$\hat{\boldsymbol{x}}_{jk+1} = \hat{\boldsymbol{x}}_{k+1/k}^{ICI} + \boldsymbol{K}_{jk+1}(z_{jk+1} - \hat{z}_{jk+1}) \tag{40}$$

⑦ Calculate the error covariance matrix as follows:

$$\boldsymbol{P}_{jk+1} = \boldsymbol{P}_{jk+1/k} - \boldsymbol{K}_{jk+1}(\boldsymbol{P}_{jk+1}^{xz})^T \tag{41}$$

4) ICI SECONDARY FUSION

① Calculate the posterior covariance square root of the system as follows:

$$\boldsymbol{P}_{k+1}^{ICI} = (\sum_{j=1}^{n} \boldsymbol{P}_{j\,k+1}^{-1} - (\sum_{j=1}^{n} \omega_j \boldsymbol{P}_{j\,k+1})^{-1})^{-1} \tag{42}$$

② Update the gain algorithm as follows:

$$L_j = \boldsymbol{P}_{k+1}^{ICI}(\boldsymbol{P}_{jk+1}^{-1} - \omega_j(\sum_{j=1}^{n} \omega_j \boldsymbol{P}_{j\,k+1})^{-1}) \tag{43}$$

③ Filter the output value as follows:

$$\hat{\boldsymbol{x}}_{k+1}^{ICI} = \sum_{j=1}^{n} L_j \hat{\boldsymbol{x}}_{jk+1} \tag{44}$$

Combined with the derived discrete state space equation, the estimation of the vehicle state parameters can be completed with the given initial values. Figure 2 shows a flow chart of the DICI-GFCKF algorithm.

V. SIMULATION ANALYSIS

To verify the estimation accuracy of the DICI-GFCKF algorithm, the GFCKF and the CKF are used as the comparison objects in this paper. By building a vehicle dynamic model on the Simulink and on the Carsim cosimulation platform, the state parameters of the vehicle are estimated in double-shift line, and the serpentine conditions to verify the superiority of the algorithm proposed in this paper.

The vehicle's partial parameters in the Carsim are as follows: the inertia moment about the Z-axis is $I_z = 2765$ kg $*\text{m}^2$; the vehicle's mass is $m = 1845$ kg; the front wheel

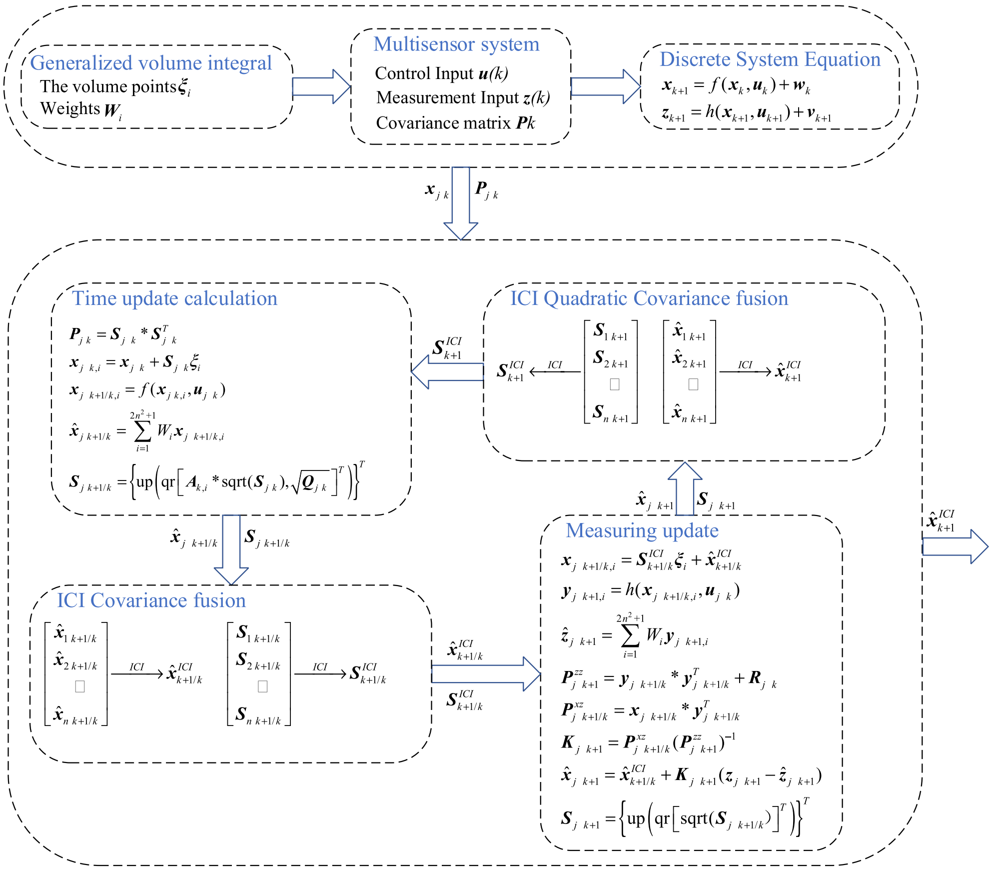

FIGURE 2. Flow chart of the DICI-GFCKF algorithm.

tread is $t_f = 1.416$ m; the rear wheel tread is $t_r = 1.375$ m; the distance between the front axle and the centroid position's center is $a = 1.402$ m; the distance between the centroid position's center and the back axle is $b = 1.546$ m; the wheel radius is $R = 0.359$ m; and the height of the center of the mass is $h_g = 0.590$ m.

In this paper, a dual-sensor system is used in the simulation to verify the effectiveness of the proposed algorithm. The following are the error covariance matrix, the process noise covariance matrix, and the measurement noise covariance matrix as follows:

$$\begin{cases} \boldsymbol{P}_{k1} = diag\left(\left[0.1^2, 0.1^2, 0.1^2, 1, 1, 1, 1\right]\right) \\ \boldsymbol{P}_{k2} = diag\left([0.1, 0.1, 0.1, 10, 10, 10, 10]\right) \\ \boldsymbol{Q}_1 = diag\left(\left[0.01^2, 0.01^2, 0.001^2, 1, 1, 1, 1\right]\right) \\ \boldsymbol{Q}_2 = diag\left(\left[0.01^2, 0.01^2, 0.01^2, 10, 10, 10, 10\right]\right) \\ \boldsymbol{R}_1 = 0.5 * diag\left([1, 1, 1]\right) \\ \boldsymbol{R}_2 = diag\left([1, 1, 1]\right) \end{cases} \tag{45}$$

The root mean square error (RMSE) is used for quantitative analysis to compare and assess the simulation results intuitively as follows:

$$RMSE(\boldsymbol{x}) = \sqrt{\frac{1}{n}\sum_{t=1}^{n}(\boldsymbol{x}(t) - \hat{\boldsymbol{x}}(t))^2} \tag{46}$$

where the actual value is $\boldsymbol{x}(t)$ and the estimated value is $\hat{\boldsymbol{x}}(t)$.

A. DOUBLE-SHIFT LINE CONDITION

With a speed of 80 km/h and a road adhesion coefficient of 0.85, the simulation experiment is run. The observer's sample time is 0.01 s. The four wheels' yaw rate, the sideslip angle, the longitudinal velocity, and the lateral force are estimated. The simulation results, the evaluation indices and the computation cost are shown in Figures 3-4 and in Tables 1-2.

The partial enlargement of Figure 3(a) shows that the value obtained with the DICI-GFCKF algorithm is closer to the actual value, and the RMSE index is better than the that of the GFCKF and the CKF by 43.04% and 65.50%, respectively. Figure 3 (b) shows that both algorithms have different degrees of divergence, and the reason for this may be that the tires enter the nonlinear area when the vehicle is cornering at high speed. The lateral stiffness of tires will change nonlinearly with the change in the vehicle's driving state. However, the tire lateral stiffness in the filter is the lateral stiffness of the vehicle during steady driving; therefore, there are some model

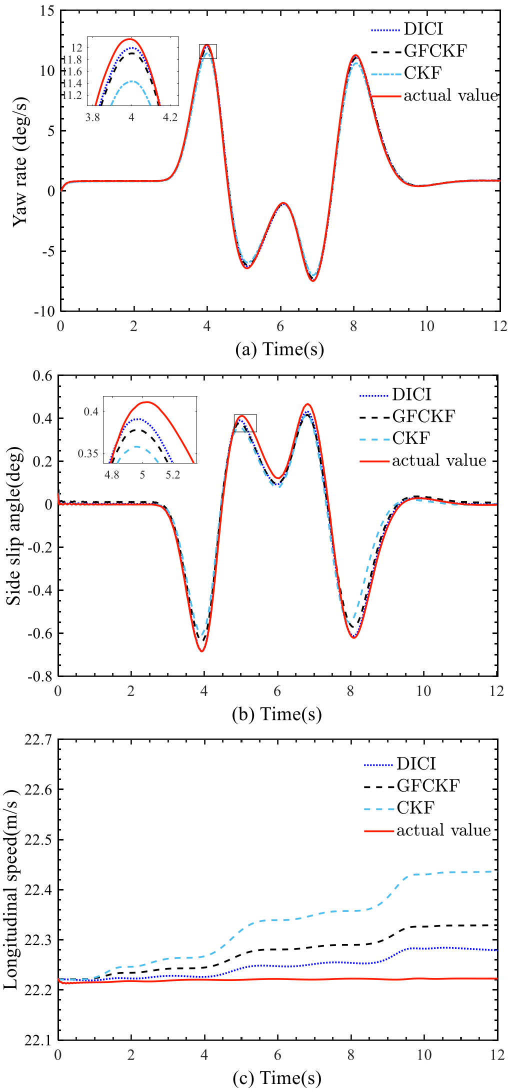

FIGURE 3. Vehicle state parameter estimation: (a) the yaw rate; (b) the sideslip angle; and (c) the longitudinal speed.

TABLE 1. Comparison of the RMSE indices under the double-shifted line condition.

Variable	$RMSE_{DICI-GFCKF}$	$RMSE_{GFCKF}$	$RMSE_{CKF}$
γ / (deg/s)	0.1047	0.1838	0.3035
β / deg	0.0231	0.0324	0.2269
F_{yfl} / N	23.5169	77.1338	101.7281
F_{yfr} / N	20.6494	75.5859	85.0141
F_{yrl} / N	54.7503	70.9130	98.0560
F_{yrr} / N	48.4509	70.6526	91.7303

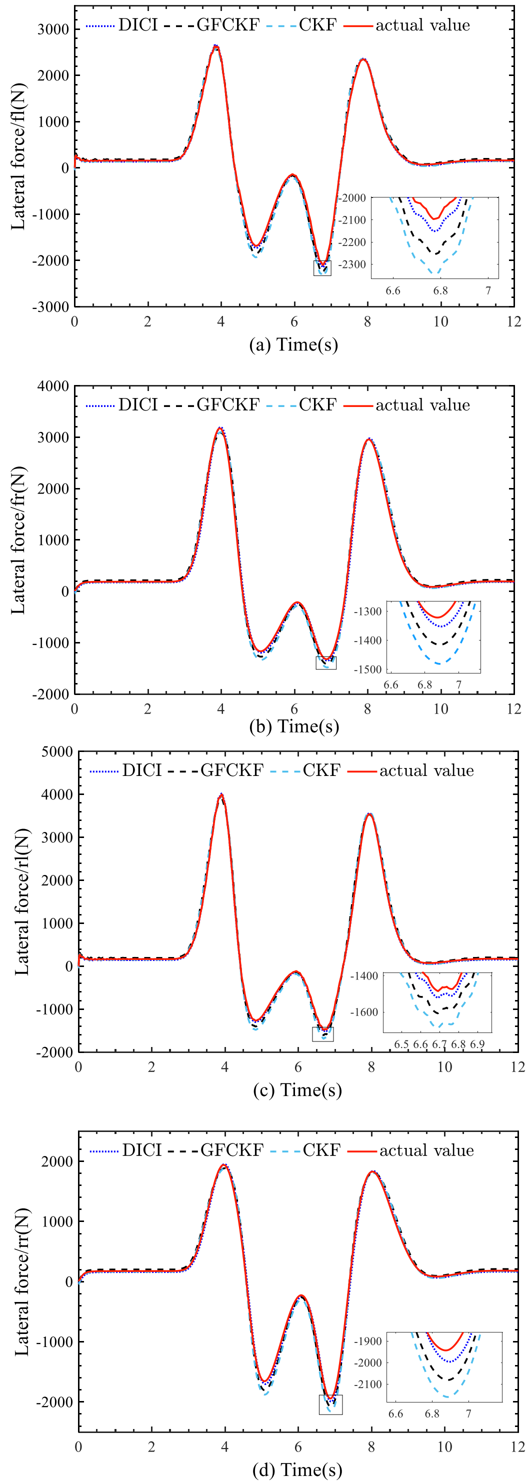

FIGURE 4. Tire lateral force estimation: (a) front left; (b) front right; (c) left rear; and (d) right rear.

errors. It is also possible to ignore the suspension design and the rolling resistance when building mathematical models. Therefore, there is a deviation between the tire angular speed of the Carsim software and that of the mathematical model. Through analysis of the RMSE index, the DICI-GFCKF algorithm is still 28.70% and 89.82% better than the GFCKF and the CKF, respectively. According to Figure 3(c), the GFCKF and the CKF diverge after 5 s, but the DICI-GFCKF algorithm proposed in this paper still maintains a stable state. This shows that the convergence of the DICI-GFCKF is better than that of the GFCKF and the CKF when the system fluctuates.

TABLE 2. Comparison of the computation cost under the double-shifted line condition.

Algorithm Name	Calls	Total Times(s)	Self Time(s)
DICI-GFCKF	24004	6.381	0.339
GFCKF	24004	6.356	0.344
CKF	24004	6.318	0.343

TABLE 3. Comparison of the RMSE indices under the serpentine condition.

Variable	$RMSE_{DICI\text{-}GFCKF}$	$RMSE_{GFCKF}$	$RMSE_{CKF}$
γ / (deg/s)	0.0946	0.1489	0.3397
β / deg	0.0103	0.0257	0.0661
F_{yfl} / N	13.0275	21.7851	46.7903
F_{yfr} / N	19.6707	22.9817	47.9505
F_{yrl} / N	16.6652	23.8255	45.2901
F_{yrr} / N	16.0632	22.5164	48.8586

TABLE 4. Comparison of the computation cost under the serpentine condition.

Algorithm Name	Calls	Total Times(s)	Self Time(s)
DICI-GFCKF	30004	7.784	0.414
GFCKF	30004	7.763	0.411
CKF	30004	7.718	0.409

As seen from the partial enlargement of Figure 4(a-d), the accuracy of the vehicle lateral force estimated by the DICI-GFCKF is better than that estimated by the GFCKF and the CKF respectively. Its RMSE evaluation indices are better than 69.1%, 72.68%, 22.79% and 31.42% of the GFCKF and 76.88%, 75.71%, 44.16% and 47.18% of the CKF, respectively. Combined with Table 1 and Table 2, the DICI-GFCKF algorithm not only improves the estimation accuracy, but also does not have too high computation cost. Its computation cost is higher than 0.025s and 0.063s of the GFCKF algorithm and the CKF algorithm.

B. THE SERPENTINR CONDITION

The speed is modified to 65 km/h, the road adhesion coefficient is 0.85, and the observer and other parameters remain unchanged to further verify the accuracy of the DICI-GFCKF algorithm. The serpentine condition is used in the simulation experiment, as illustrated in Figures 5-6.

Figures (5-6) show that the error between the estimated and the actual values of both algorithms is small. Through local enlargement, the estimated value of the DICI-GFCKF algorithm is closer to the actual value than that of the GFCKF and the CKF. Figure 5(a) and Figure 5(b) show that the estimation accuracy of both algorithms is high. Table 3 shows that the RMSE index of the DICI-GFCKF algorithm is smaller than that of the GFCKF algorithm and the CKF algorithm. In addition, the RMSE index is 36.47%, 59.92%, 72.15%, and 84.42% better than that of the GFCKF and the CKF, respectively. Figure 5(c) shows that within 0∼5 s from the beginning of the simulation, the observation results of both algorithms are accurate. However, after 5 s, all algorithms also have errors that continue to expand. The figure shows that the estimation accuracy of the DICI-GFCKF algorithm is always better than that of the GFCKF and the CKF.

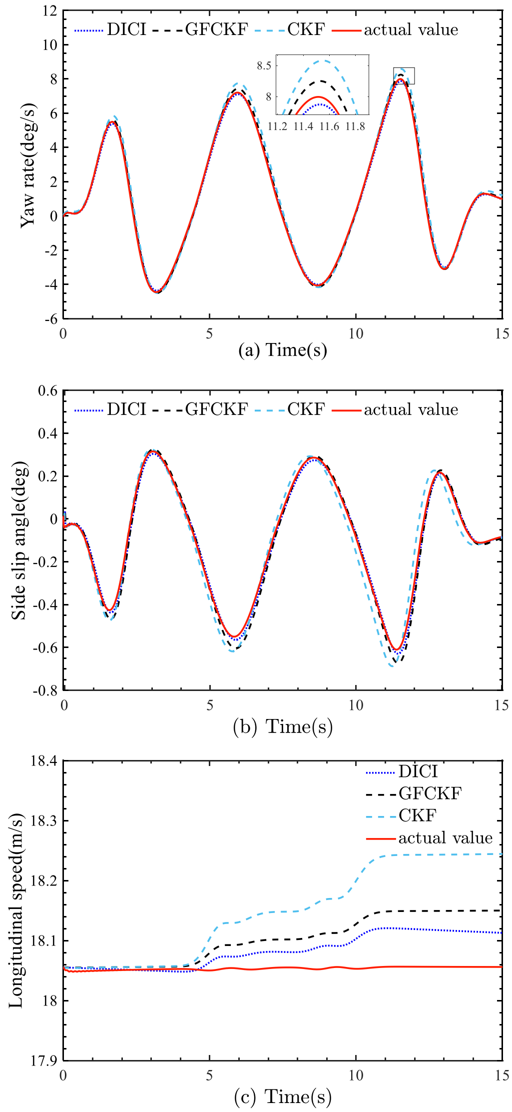

FIGURE 5. Vehicle state parameter estimation: (a) the yaw rate; (b) the sideslip angle; and (c) the longitudinal speed.

An analysis of the situation in Figure 5(c) shows that when the vehicle is driving in the curve under the serpentine condition, the steering wheel and the front wheel angles have a large sudden change in a short time. Lateral acceleration and tire lateral stiffness also change. These dynamic characteristics exacerbate the nonlinearity of the vehicle system and introduce some model errors into the algorithm estimation. Therefore, in Figure 5(c), the two algorithms have different degrees of errors, which also indicates that when nonlinear changes occur in the system, the robustness of the

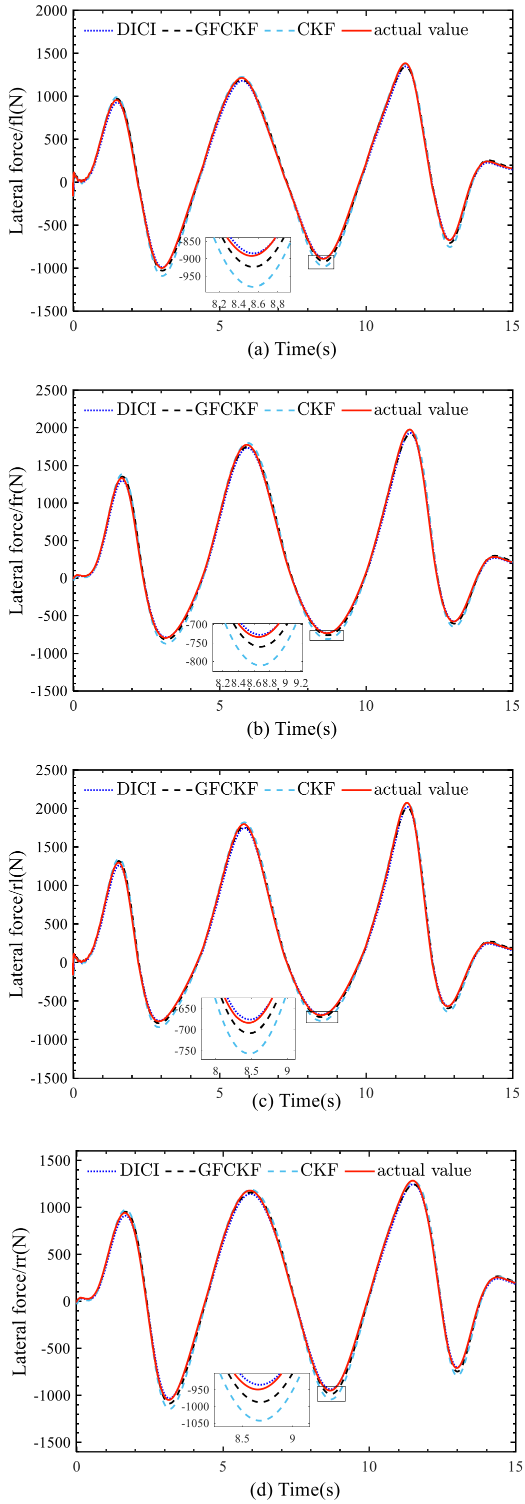

FIGURE 6. Tire lateral force estimation: (a) front left; (b) front right; (c) left rear; and (d) right rear.

DICI-GFCKF algorithm is higher than that of the GFCKF and the CKF.

As seen from the local enlargements of Figure 6(a-d), in the estimation of tire lateral force under the serpentine conditions, the DICI-GFCKF has higher accuracy than the GFCKF and the CKF, and its RMSE evaluation indices are better than 40.20%, 14.41%, 30.05%, and 28.66% of the GFCKF and 72.16%, 58.98%, 63.20% and 67.23% of the CKF, respectively. It can be seen from Table 4 that the computation cost of the DICI-GFCKF algorithm is 0.021 and 0.066 higher than that of the GFCKF algorithm and the CKF algorithm respectively.

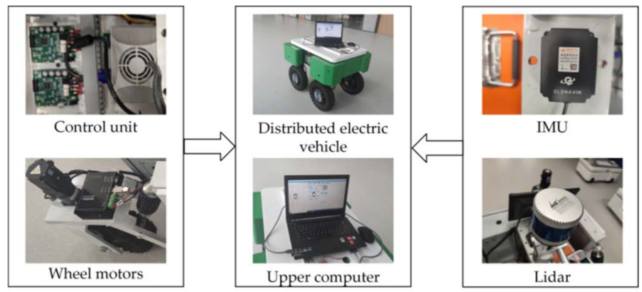

FIGURE 7. Distributed electric vehicle experiment platform.

TABLE 5. Comparison of the RMSE indices under the double-shifted line condition.

Variable	$RMSE_{DICI\text{-}GFCKF}$	$RMSE_{GFCKF}$	$RMSE_{CKF}$
v_x / (km/h)	0.2838	0.4798	0.9353
γ / (deg/s)	0.3055	0.7880	1.0348
β / deg	0.0637	0.1461	0.1946

VI. VEHICLE EXPERIMENT

To further verify the feasibility of the DICI-GFCKF algorithm, a road experiment is carried out on the distributed electric vehicle experiment platform, which is shown in Figure 7. LiDAR is used to establish the double-shift line conditions and the serpentine conditions on the upper computer, taking the vehicle motion parameters collected by the IMU (inertial measurement unit) as true values. The estimated values of the DICI-GFCKF algorithm are compared with the actual value to verify the validity of the algorithm.

Based on the existing actual vehicle experiment conditions, only the longitudinal velocity, the yaw rate, and the sideslip angle are tested in this experiment. The effectiveness of the DICI-GFCKF algorithm in the medium- and high-speed domains is verified in the co-simulation experiments. Considering the safety of the actual vehicle experiment, the initial speed is set at 30 km/h on the road surface with an adhesion coefficient of 0.8.

The actual vehicle experiment results under the double-shift line conditions are shown in Figure 8:

The actual vehicle experiment results under the serpentine conditions are shown in Figure 9.

To better analyze the experimental results, the root mean square error (RMSE) index is used to process the observation results of the two groups, as shown in Tables 5-6.

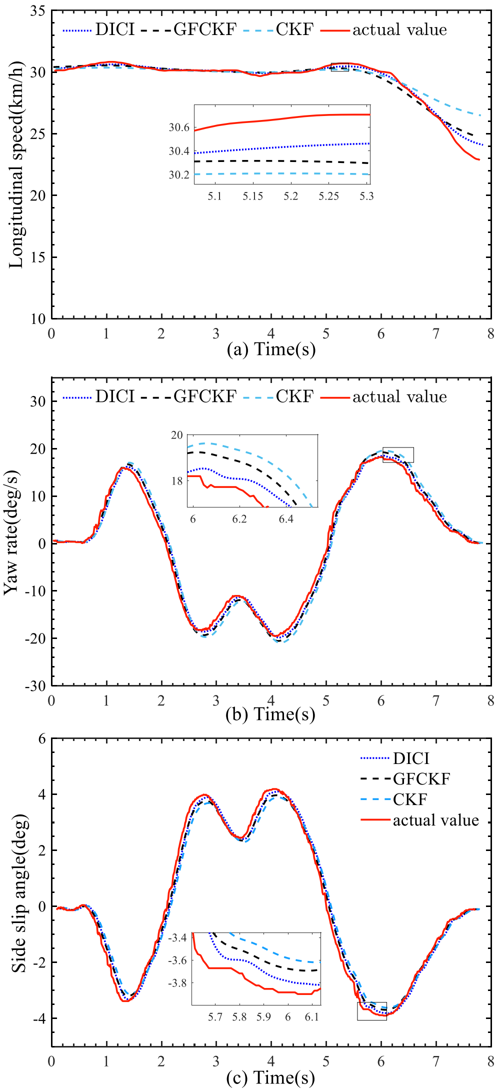

FIGURE 8. Results of the actual vehicle experiment under the double-shift line condition.

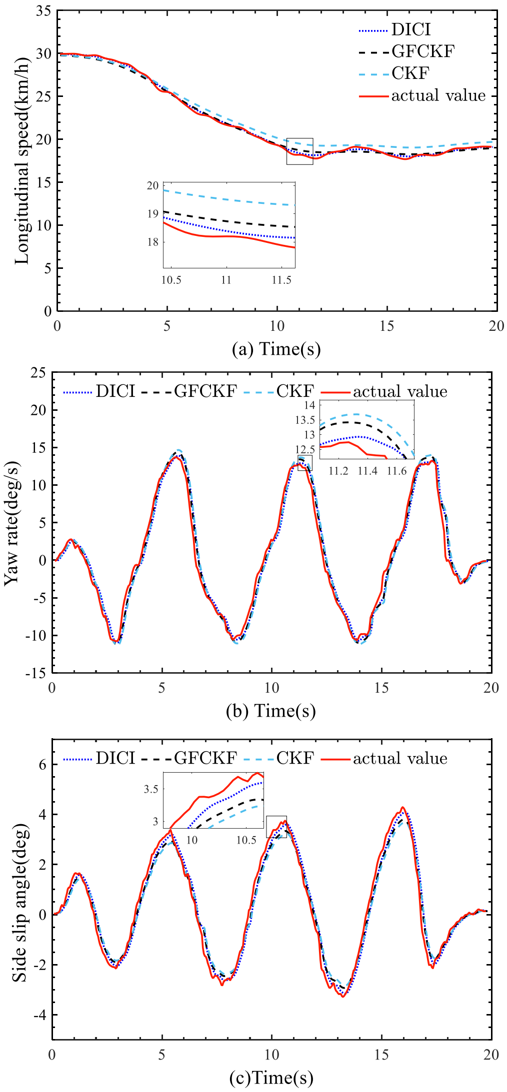

FIGURE 9. Results of the actual vehicle experiment under the serpentine conditions.

TABLE 6. Comparison of the RMSE indices under the serpentine condition.

Variable	$RMSE_{DICI-GFCKF}$	$RMSE_{GFCKF}$	$RMSE_{CKF}$
v_x / (km/h)	0.1560	0.3352	0.7420
γ / (deg/s)	0.2405	0.5665	0.8871
β / deg	0.0880	0.2215	0.2759

As shown in Figure 8 (a) and Figure 9 (a), the vehicle speed decreases over the course of the experiment. The DICI-GFCKF algorithm does not diverge due to the decrease in the vehicle speed, while the GFCKF algorithm and the CKF algorithm show a larger divergence after 5 s, as shown in Figure 8(a). This shows that the DICI-GFCKF algorithm has high robustness and accuracy, and their RMSEs are better than those of the GFCKF and the CKF by 40.85%, 53.46%, 69.65%, and 78.98%.

Figure 8 (b-c) and Figure 9 (b-c) show the situation where the vehicle is driven at a low speed at the turning of the double-shift line and under the serpentine conditions. The DICI-GFCKF algorithm does not produce large errors due to the sudden changes in the steering wheel and the front wheel angle. However, the estimated value of the GFCKF and the CKF have a large deviation compared with the value from the actual vehicle experiment. The results show that the DICI-GFCKF algorithm is better than the GFCKF algorithm and the CKF algorithm in estimating vehicle state parameters, and their RMSEs are 61.23%, 56.40%, 57.55%, 60.27% and 70.48%, 67.27%, 72.89%, and 68.10% better than those of the GFCKF and the CKF.

The actual vehicle experiment results again verify that the DICI-GFCKF algorithm proposed in this paper has high estimation accuracy and robustness.

VII. CONCLUSION

In this paper, a new estimation algorithm is proposed for the traditional vehicle state parameter estimation algorithm. The generalized cubature rule is used to improve the fifth-order CKF, and the ICI fusion algorithm is added in the update process to improve the estimation accuracy of the algorithm. The robustness of the DICI-GFCKF algorithm is verified on the MATLAB/Simulink and Carsim cosimulation platforms.

The virtual experiments under the double-shift line condition and the serpentine working condition show that the errors between the estimated value of the DICI-GFCKF algorithm and the reference value are small. The estimation errors of the GFCKF and the CKF are slightly larger than those of the DICI-GFCKF algorithm, especially at the peak of the estimation curve. The RMSE index introduced further shows that the estimation ability of the DICI-GFCKF algorithm is superior to that of the GFCKF and the CKF overall.

Through the limited experimental conditions, the actual car experiment of the DICI-GFCKF algorithm is carried out. The DICI-GFCKF algorithm is verified again with high accuracy and robustness. It can adapt well to the harsh environment of vehicle driving, and the practical application prospects are broad.

REFERENCES

[1] Z. Yixi, M. Jian, Z. Xuan, Z. Kai, and L. Xiaodong, "Unscented Kalman filter estimator of vehicle states and parameters based on ant lion optimization algorithm," *China J. Highway Transp.*, vol. 33, no. 5, pp. 165–177, 2020.

[2] S. Habib, M. M. Khan, F. Abbas, L. Sang, M. U. Shahid, and H. Tang, "A comprehensive study of implemented international standards, technical challenges, impacts and prospects for electric vehicles," *IEEE Access*, vol. 6, pp. 13866–13890, 2018.

[3] X. Jin, G. Yin, and N. Chen, "Advanced estimation techniques for vehicle system dynamic state: A survey," *Sensors*, vol. 19, no. 19, p. 4289, Oct. 2019.

[4] Y. Song, H. Shu, X. Chen, and S. Luo, "Direct-yaw-moment control of four-wheel-drive electrical vehicle based on lateral tyre–road forces and sideslip angle observer," *IET Intell. Transp. Syst.*, vol. 13, no. 2, pp. 303–312, Feb. 2019.

[5] B. L. Boada, D. Garcia-Pozuelo, M. J. L. Boada, and V. Diaz, "A constrained dual Kalman filter based on pdf truncation for estimation of vehicle parameters and road bank angle: Analysis and experimental validation," *IEEE Trans. Intell. Transp. Syst.*, vol. 18, no. 4, pp. 1006–1016, Apr. 2017.

[6] S. Yitong, S. Hongyu, C. Xianbao, J. Changqing, and G. Cheng, "State and parameters estimation for distributed drive electric vehicle based on unscented Kalman filter," *J. Mech. Eng.*, vol. 56, no. 16, pp. 204–213, 2020.

[7] Z. Wanzhong, Z. Han, and W. Chunyan, "Estimation of vehicle state parameters based on unscented Kalman filtering," *J. South China Univ. Technol., Natural Sci. Ed.*, vol. 44, no. 3, pp. 76–80 and 88, 2016.

[8] H. Jung and S. B. Choi, "Real-time individual tire force estimation for an all-wheel drive vehicle," *IEEE Trans. Veh. Technol.*, vol. 67, no. 4, pp. 2934–2944, Apr. 2018.

[9] T. Chen, X. Xu, L. Chen, H. Jiang, Y. Cai, and Y. Li, "Estimation of longitudinal force, lateral vehicle speed and yaw rate for four-wheel independent driven electric vehicles," *Mech. Syst. Signal Process.*, vol. 101, pp. 377–388, Feb. 2018.

[10] X. Xinfa, Y. Xiujian, and Z. Kun, "Estimation of sideslip angle based on extended Kalman filter," *Agricult. Equip. Vhicle Eng.*, vol. 56, no. 3, pp. 60–63 and 67, 2018.

[11] Z. Rongyun, G. Changfu, S. Peicheng, Z. Linfeng, and Z. Changsheng, "Research on chaos control of permanent magnet synchronous motor based on the synthetical sliding mode control of inverse system decoupling," *J. Vib. Control*, vol. 27, nos. 9–10, pp. 1009–1019, May 2021.

[12] Z. Rongyun, G. Changfu, S. Peicheng, Z. Linfeng, Z. Changsheng, and W. Chen, "The permanent magnet synchronous motor sensorless control of electric power steering based on iterative fifth-order cubature Kalman filter," *J. Dyn. Syst., Meas., Control*, vol. 142, no. 8, Aug. 2020, Art. no. 081004.

[13] J. Zhu, Z. Wang, L. Zhang, and W. Zhang, "State and parameter estimation based on a modified particle filter for an in-wheel-motor-drive electric vehicle," *Mechanism Mach. Theory*, vol. 133, pp. 606–624, Mar. 2019.

[14] V. Elvira, J. Miguez, and P. M. Djurić, "On the performance of particle filters with adaptive number of particles," *Statist. Comput.*, vol. 31, no. 6, pp. 1–18, Nov. 2021.

[15] H. Heidfeld, M. Schünemann, and R. Kasper, "UKF-based state and tire slip estimation for a 4WD electric vehicle," *Vehicle Syst. Dyn.*, vol. 58, no. 10, pp. 1479–1496, Oct. 2020.

[16] J. Xianjian, Y. Junpeng, Y. Guodong, W. Jinxiang, C. Nan, and L. Yanbo, "Combined state and parameter observation of distributed drive electric vehicle via dual unscented Kalman filter," *J. Mech. Eng.*, vol. 55, no. 22, pp. 93–102, 2019.

[17] T. Kim and T.-H. Park, "Extended Kalman filter (EKF) design for vehicle position tracking using reliability function of radar and lidar," *Sensors*, vol. 20, no. 15, p. 4126, Jul. 2020.

[18] W. Shaoyuan, X. Runchun, and L. Gang, "Study on vehicle driving state estimation based on cubature Kalman filter," *Machinery Des. Manuf.*, vol. 53, pp. 69–73, Jan. 2015.

[19] A. Katriniok and D. Abel, "Adaptive EKF-based vehicle state estimation with online assessment of local observability," *IEEE Trans. Control Syst. Technol.*, vol. 24, no. 4, pp. 1368–1381, Jul. 2016.

[20] S. Strano and M. Terzo, "Constrained nonlinear filter for vehicle sideslip angle estimation withno a priori knowledge of tyre characteristics," *Control Eng. Pract.*, vol. 71, pp. 10–17, Feb. 2018.

[21] I. Arasaratnam and S. Haykin, "Cubature Kalman filters," *IEEE Trans. Autom. Control*, vol. 54, no. 6, pp. 1254–1269, May 2009.

[22] L. Gang, "Estimation of vehicle state and road adhesion coefficient based on Kalman filter," *J. South China Univ. Technol., Natural Sci. Ed.*, vol. 42, no. 8, pp. 129–135, 2014.

[23] F. Xiansheng, G. Xiuqing, L. Lingquan, and L. Zuoshi, "Vehicle state parameter estimation based on fuzzy adaptive unscented Kalman filter," *Mod. Manuf. Eng.*, vol. 43, no. 7, pp. 25–30, Jul. 2020.

[24] Z. Bing, Q. Xiang, W. Xiaojian, and L. Lefei, "AFS control based on estimation of vehicle state and road coefficient using UKF method," *J. Hunan Univ., Natural Sci.*, vol. 46, no. 8, pp. 1–8, 2019.

[25] Z. Zhida, Z. Ling, Z. Zhiwei, L. Yinong, and L. Yixiao, "Lateral trajectory tracking control of intelligent vehicle based on adaptive model prediction," *China J. Highway Transp.*, vol. 24, pp. 1–13, Jun. 2021.

[26] X. Ding, Z. Wang, L. Zhang, and C. Wang, "Longitudinal vehicle speed estimation for four-wheel-independently-actuated electric vehicles based on multi-sensor fusion," *IEEE Trans. Veh. Technol.*, vol. 69, no. 11, pp. 12797–12806, Nov. 2020.

[27] W. Long, Y. Guodong, G. Keke, D. Haoxuan, L. Yanbo, and Z. Fengjiao, "Tire tateral forces and sideslip angle estimation for distributed drive electric vehicle using noise adaptive cubature Kalman filter," *J. Mech. Eng.*, vol. 55, no. 20, pp. 103–112, 2019.

[28] G. Xiaoyang, W. Gang, W. Wanpeng, and W. Run, "Inverse covariance intersection fusion robust steady-state Kalman filter," *J. Air Force Eng. Univ., Natural Sci. Ed.*, vol. 20, no. 2, pp. 94–97, 2019.

[29] D. Meng, L. Miao, H. Shao, and J. Shen, "A seventh-degree cubature Kalman filter," *Asian J. Control*, vol. 20, no. 1, pp. 250–262, Jan. 2018.

[30] J.-C. Santos-León, R. Orive, D. Acosta, and L. Acosta, "The cubature Kalman filter revisited," *Automatica*, vol. 127, May 2021, Art. no. 109541.

[31] M. V. Kulikova and G. Y. Kulikov, "MATLAB-based general approach for square-root extended-unscented and fifth-degree cubature Kalman filtering methods," *Eur. J. Control*, vol. 59, pp. 1–12, May 2021.

[32] S. Y. Kim, C. H. Kang, and J. W. Song, "1-point RANSAC UKF with inverse covariance intersection for fault tolerance," *Sensors*, vol. 20, no. 2, p. 353, Jan. 2020.

[33] C. H. Kang, S. Y. Kim, and J. W. Song, "Data fusion with inverse covariance intersection for prior covariance estimation of the particle flow filter," *IEEE Access*, vol. 8, pp. 221203–221213, 2020.

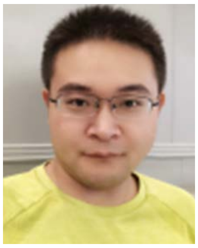

ZHANG RONGYUN received the B.S. (Eng.) and Ph.D. degrees in vehicle engineering from the Hefei University of Technology, China, in June 2009 and June 2015, respectively. He is currently an Associate Professor with the School of Mechanical Engineering, Anhui Polytechnic University, China. His research interests include vehicle safety control, vehicle intelligent control, PMSM control, and electric vehicle technology.

LIU YAMING received the B.Eng. degree in vehicle engineering from Anhui Polytechnic University, in 2020, where he is currently pursuing the master's degree in automotive engineering. His research interest includes electric vehicle state parameter estimation.

SHI PEICHENG received the Ph.D. degree in vehicle engineering from the Hefei University of Technology, in 2010. He is currently a Professor with the School of Mechanical Engineering, Anhui Polytechnic University, China, where he is also working with the School of Mechanical Engineering. His research interests include vibration and control of machinery and automobile vibration.

ZHAO LINFENG received the Ph.D. degree from the Hefei University of Technology, Hefei, China, in 2010. He is currently an Associate Professor with the School of Automotive and Transportation Engineering, Hefei University of Technology. His current research interests include vehicle dynamics and control, electric power steering systems, and intelligent vehicles.

DU YUFENG received the B.Eng. degree in material forming and control engineering from the College of Mechanical & Electrical Engineering, Anhui Polytechnic University, in 2019, where he is currently pursuing the master's degree in automotive engineering. His research interests include intelligent networked vehicle, machine learning, and computer vision.

FENG YONGLE received the B.Eng. degree in vehicle engineering from the College of Mechanical & Electrical Engineering, Anhui Polytechnic University, in 2020, where he is currently pursuing the master's degree in automotive engineering. His research interests include vehicle dynamics control, path planning, and path tracking.